The Astrophysical Journal Letters, 901:L20 (9pp), 2020 October 1 https://doi.org/10.3847/2041-8213/abb462


# Limits on Precursor and Afterglow Radio Emission from a Fast Radio Burst in a Star-forming Galaxy

Shivani Bhandari[1], Keith W. Bannister[1], Emil Lenc[1], Hyerin Cho[2], Ron Ekers[1,3], Cherie K. Day[1,4], Adam T. Deller[4], Chris Flynn[4], Clancy W. James[3], Jean-Pierre Macquart[3,12], Elizabeth K. Mahony[1], Lachlan Marnoch[1,5,6], Vanessa A. Moss[1,7], Chris Phillips[1], J. Xavier Prochaska[8,9], Hao Qiu[1,7], Stuart D. Ryder[5,6], Ryan M. Shannon[4], Nicolas Tejos[10], and O. Ivy Wong[11]

[1] Australia Telescope National Facility, CSIRO Astronomy and Space Science, P.O. Box 76, Epping, NSW 1710, Australia; shivani.bhandari@csiro.au
[2] School of Physics and Chemistry, Gwangju Institute of Science and Technology, Gwangju, 61005, Republic of Korea
[3] International Centre for Radio Astronomy Research, Curtin University, Bentley, WA 6102, Australia
[4] Centre for Astrophysics and Supercomputing, Swinburne University of Technology, John Street, Hawthorn, VIC 3122, Australia
[5] Department of Physics and Astronomy, Macquarie University, North Ryde, NSW 2109, Australia
[6] Research Centre for Astronomy, Astrophysics & Astrophotonics, Macquarie University, North Ryde, NSW 2109, Australia
[7] Sydney Institute for Astronomy, School of Physics, University of Sydney, Sydney, NSW 2006, Australia
[8] University of California, Santa Cruz, 1156 High Street, Santa Cruz, CA 95064, USA
[9] Kavli Institute for the Physics and Mathematics of the Universe (Kavli IPMU), 5-1-5 Kashiwanoha, Kashiwa, 277-8583, Japan
[10] Instituto de Física, Pontificia Universidad Católica de Valparaíso, Casilla 4059, Valparaíso, Chile
[11] CSIRO Astronomy & Space Science, P.O. Box 1130, Bentley, WA 6102, Australia
*Received 2020 July 26; revised 2020 August 30; accepted 2020 September 2; published 2020 September 24*

## Abstract

We present a new fast radio burst (FRB) at 920 MHz discovered during commensal observations conducted with the Australian Square Kilometre Array Pathfinder (ASKAP) as part of the Commensal Real-time ASKAP Fast Transients (CRAFT) survey. FRB 191001 was detected at a dispersion measure (DM) of 506.92(4) pc cm$^{-3}$ and its measured fluence of 143(15) Jy ms is the highest of the bursts localized to host galaxies by ASKAP to date. The subarcsecond localization of the FRB provided by ASKAP reveals that the burst originated in the outskirts of a highly star-forming spiral in a galaxy pair at redshift $z = 0.2340(1)$. Radio observations show no evidence for a compact persistent radio source associated with the FRB 191001 above a flux density of 15 $\mu$Jy. However, we detect diffuse synchrotron radio emission from the disk of the host galaxy that we ascribe to ongoing star formation. FRB 191001 was also detected as an image-plane transient in a single 10 s snapshot with a flux density of 19.3 mJy in the low-time-resolution visibilities obtained simultaneously with CRAFT data. The commensal observation facilitated a search for repeating and slowly varying radio emissions 8 hr before and 1 hr after the burst. We found no variable radio emission on timescales ranging from 1 ms to 1.4 hr. We report our upper limits and briefly review FRB progenitor theories in the literature that predict radio afterglows. Our data are still only weakly constraining of any afterglows at the redshift of the FRB. Future commensal observations of more nearby and bright FRBs will potentially provide stronger constraints.

*Unified Astronomy Thesaurus concepts:* Radio continuum emission (1340); Interferometers (805); Polarimetry (1278); Starburst galaxies (1570)

## 1. Introduction

Fast radio bursts (FRBs) are energetic bursts of radio emission that last for tens of microseconds to tens of milliseconds (Lorimer et al. 2007) and originate at cosmological distances (Chatterjee et al. 2017; Bannister et al. 2019; Ravi et al. 2019). More than 20 FRB sources have been observed to emit repeat pulses (Spitler et al. 2016; Andersen et al. 2019; Kumar et al. 2019), allowing some of them to be localized to host galaxies via targeted follow-up with radio interferometers (Tendulkar et al. 2016; Marcote et al. 2020).

The bulk of the ~100-strong population of published FRBs, however, are single-burst events. The transition from finding such events with single dishes to with interferometric arrays capable of imaging the received FRB emission has resulted in (sub)arcsecond localization in recent detections (Bannister et al. 2019; Prochaska et al. 2019; Ravi et al. 2019; Law et al. 2020; Macquart et al. 2020), revealing their host galaxies and in some cases even to sites within the hosts (Bhandari et al. 2020).

Analyses of the host environments of localized repeating and nonrepeating FRBs and high brightness temperatures of the bursts tend to favor models involving compact objects such as white dwarfs (WDs), neutron stars (NSs), and black holes (BHs) (Liu 2018; Wang & Lai 2020; Wang et al. 2020; Murase et al. 2018). Some of these models predict radio afterglows accompanying an FRB with timescales of days to years and apparent luminosities as high as sub-mJy levels in favorable circumstances.

Margalit et al. (2019) predicted late-time (months to years) radio emission accompanying FRBs from magnetars born in binary neutron star mergers and accretion-induced collapse (AIC) of a WD through the interaction of the ejecta with the surrounding local interstellar medium. It is also proposed that the magnetospheric instability of an isolated or a binary rotating black hole may result in FRBs and their afterglows (Liu et al. 2016). If FRBs are related to gamma-ray bursts (GRBs; Zhang 2014), the radio afterglow may last from hours to years as reverse and forward shocks interact with ejecta and the interstellar medium (Frail 2003). Yi et al. (2014) also predicted the optical, radio, and high-energy afterglow light curves for forward and reverse-shock emission resulting from FRBs. They concluded that FRB afterglows are too faint to be detected by current detectors.

[12] Deceased.

While theoretical predictions for radio afterglows are plentiful, observational evidence is scant. An initially promising candidate was identified from radio follow-up conducted within ∼2 hr of the Parkes FRB 150418, reporting fading radio emission in the field (Keane et al. 2016). Subsequent observations showed that scintillation of an unassociated active galactic nucleus (AGN) was a more plausible explanation (Williams & Berger 2016; Johnston et al. 2017). In 2018, multiwavelength follow-up of three real-time FRBs did not detect any afterglows in radio or other wavelengths (Bhandari et al. 2018b). Potential explanations include FRBs having fainter radio afterglows (less than 50 $\mu$Jy at 3$\sigma$), these afterglows evolving on timescales faster than what had been surveyed (less than a day), or FRBs not producing afterglows. Deeper follow-up observations of a larger sample of FRBs are needed to address the first possibility, but the second is best addressed through observations where radio imaging is being performed during the same observation in which the FRB is discovered.

Since mid-2019, FRB searches with the Commensal Real-time Australian Square Kilometre Array Pathfinder (ASKAP) Fast Transients Survey (CRAFT; Macquart et al. 2010) have started to operate simultaneously with other survey science projects undertaken with ASKAP. In contrast to previously reported CRAFT detections (Bannister et al. 2019; Prochaska et al. 2019; Macquart et al. 2020), during commensal operations, the regular ASKAP correlator is still running and producing low-time-resolution visibility products needed for regular ASKAP imaging. The simultaneous operation of the ASKAP hardware correlator and ASKAP-CRAFT system is powerful in probing long-timescale radio emission before and after the FRB itself. FRB 191001 was the first event to be detected during such an observation, facilitating a deep search for slowly varying ($\geqslant$10 s) radio emission within hours before and after the FRB.

In this Letter we report the detection and localization of FRB 191001 to its host galaxy along with a search for radio emission pre- and post-FRB. The detection and properties of the FRB and its host galaxy are presented in Section 2, and the results of our search for radio emission from the host galaxy at the location of the FRB in Section 3. In Section 4, we discuss the implications of our findings, and we conclude and provide a summary in Section 5.

## 2. Properties of FRB 191001 and Its Host Galaxy

### 2.1. Discovery of FRB 191001

The burst was detected on 2019 October 1 UT 16:55:35.97081 at a dispersion measure (DM) of 506.92(4) pc cm$^{-3}$, during observations taken as part of the Evolutionary Map of the Universe (EMU; Norris et al. 2011) pilot survey in the frequency range of 752–1088 MHz. EMU is an ASKAP key science project to conduct a deep radio continuum survey of the entire southern sky. The FRB was detected in beam 24 (an outer ASKAP beam) of the closepack36 beam footprint pattern (see Shannon et al. 2018) during a ∼9 hr observation with 30 antennas in a 336 MHz band centered on 920 MHz. The properties of the burst are presented in Table 1. Figure 1 shows FRB 191001's pulse profile and dynamic spectrum. The discussions of the profile are presented in Section 2.5.1.

### 2.2. Commensal Low-time-resolution Observations

The standard ASKAP hardware correlator integrates and writes out visibilities on a 10 s timescale—hereafter termed "low-time-resolution" data. The correlator was operating simultaneously, and independently of, the CRAFT FRB search. The low-time-resolution data were calibrated following the standard data reduction steps as presented in Bhandari et al. (2018a) and were then used for imaging. We performed difference imaging of the consecutive 10 s snapshots around the FRB arrival time derived from the CRAFT data to check for any significant source in the direction of the FRB. FRB 191001 was detected in a difference image providing a preliminary position. Once found, we performed the imaging and deconvolution of that single integration (without differencing) to obtain a better estimate of the flux density. The FRB was detected with 9$\sigma$ significance with a primary-beam-corrected flux density of 19.3 mJy averaged over 10 s (see the right panel of Figure 2). We note that the fluence derived from the above flux density is ∼1.5× higher than the measured fluence of the FRB. This can be explained by high uncertainty in the measurement of FRB fluence because of an outer beam detection.

**Table 1**
Measured and Derived Properties of FRB 191001 and Its Host Galaxy

| Properties | |
|---|---|
| FRB | |
| Arrival time (UT)[a] at 919.5 MHz | 16:55:35.97081 |
| Incoherent S/N | 62 |
| Coherent S/N | 192 |
| Primary detection beam | 24 |
| Detection DM (pc cm$^{-3}$) | 506.92(4) |
| Structure maximized DM[b] (pc cm$^{-3}$) | 507.90(7) |
| $DM_{ISM}$ NE2001 (pc cm$^{-3}$) | 44 |
| $DM_{ISM}$ YMW16 (pc cm$^{-3}$) | 31 |
| $DM_{cosmic}$ (pc cm$^{-3}$) | $373_{(NE2001)}$ |
| R.A. (J2000) | 21:33:24.373(6) |
| Decl.(J2000) | −54:44:51.86(13) |
| Fluence[c] (Jy ms) | 143(15) |
| Modeled pulse width[d] (ms) | 0.22(3) |
| Scattering time at 824 MHz (ms) | 3.3(2) |
| Scintillation bandwidth (kHz) | ∼600 |
| Pulse rise time ($\mu$s) | ∼640 |
| Rotation measure (RM) (rad m$^{-2}$) | 55.5(9) |
| Total polarization fraction (P/I) | 58(1)% |
| Linear polarization fraction (L/I) | 57(1)% |
| Circular polarization fraction (V/I) | −5(1)% |
| Spectral energy density[a] (erg Hz$^{-1}$) | $2 \times 10^{32}$ |
| Persistent source, radio luminosity at 5.5 GHz (W Hz$^{-1}$) | $2 \times 10^{21}$ |
| Host galaxy[e] | |
| Redshift | 0.2340(1) |
| Stellar mass ($M_{\odot}$) | $5(2) \times 10^{10}$ |
| $E(B-V)$ | 0.27(16) |

**Notes.**
[a] The statistical uncertainty on the burst arrival time assumes a model for the burst morphology.
[b] https://github.com/danielemichilli/DM_phase/blob/master/DM_phase.py.
[c] Derived from 336 MHz bandwidth CRAFT intensity data.
[d] The primary pulse component width.
[e] See Heintz et al. (2020) for details about optical properties.

### 2.3. Localization of FRB 191001

The real-time detection of FRB 191001 in online incoherent-sum data triggered the retention of 3.1 s of raw (voltage) data around the FRB event. Due to a greater-than-usual latency

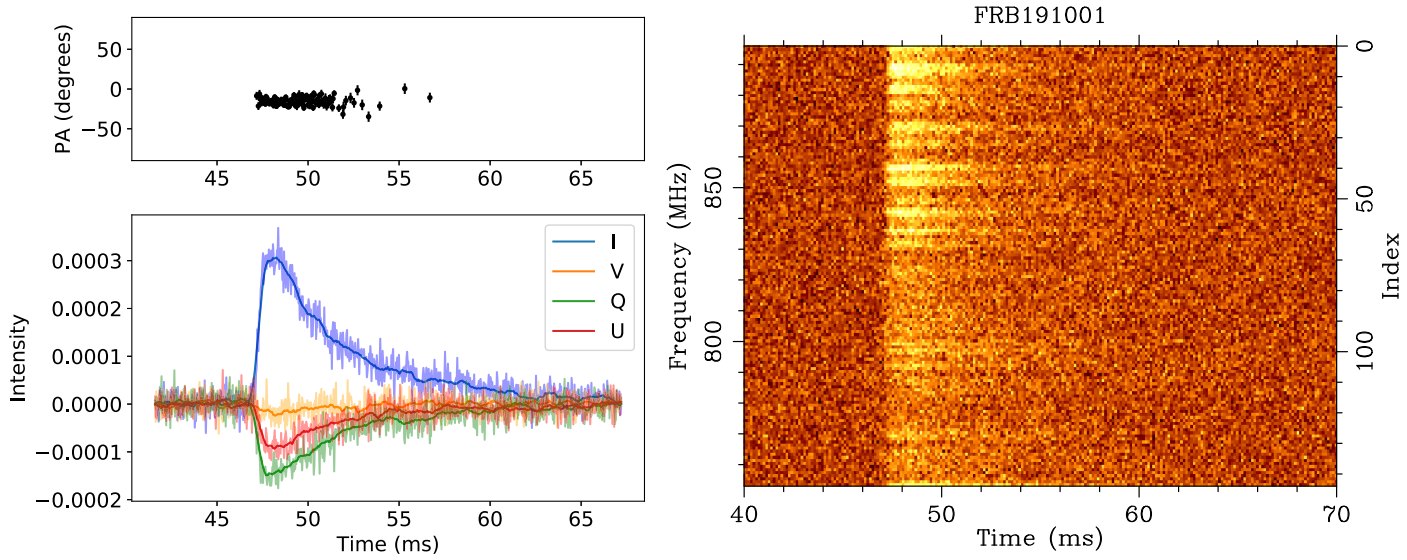


**Figure 1.** Left: the top panel shows the polarization position angle (above $4\sigma$), which is observed to be flat across the majority of the pulse, and the bottom panel shows Stokes parameter pulse profiles for FRB 191001 at 824 MHz (see Section 2.3 for details about the center frequency). The profiles represent a time resolution of 32 $\mu$s, and overplotted are 20× smoothed profiles. The FRB shows significant scattering with a scattering time of 3.3 ms at 824 MHz. Right: the dynamic spectrum of FRB 191001. The data are coherently de-dispersed at a DM of 507.90(7) pc cm$^{-3}$. The scintillation bandwidth for the burst is ∼600 kHz at 824 MHz, which is consistent with predictions for diffractive scintillation induced by the Milky Way interstellar medium (ISM; Cordes & Lazio 2002; see Section 2.5 for details).

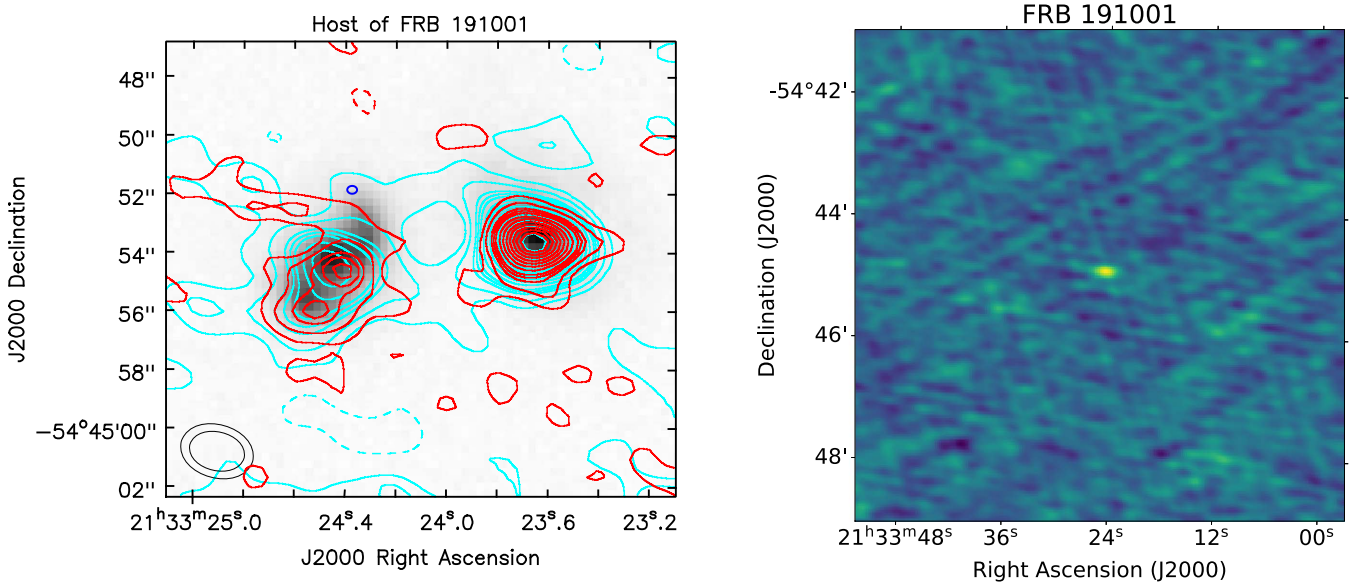


**Figure 2.** Left: background $g$-band VLT/FORS2 image of the host of FRB 191001 at a redshift of 0.2340. The blue ellipse marks the $1\sigma$ uncertainty in the position of FRB 191001, which is 165 mas in R.A. and 127 mas in decl. Cyan and red are the contours of radio emission detected with ATCA at 5.5 GHz and 7.5 GHz, respectively, in levels of [−3, 1.5, 3, 5, 6, 7, 9, 11, 13, 15, 17, 19, 21, 25, 30, 35] times the noise of ∼6 $\mu$Jy beam$^{-1}$ (see Section 2.7 for details). Right: detection of FRB 191001 in the image plane with a 10 s ASKAP snapshot obtained during commensal EMU observations. The FRB is the bright source at the image center with a primary-beam-corrected flux density of 19.3 mJy (see Section 2.2 for details).

(2.1 s in this case) between the FRB arrival and the voltage dump trigger,[13] only half the FRB signal was captured (a center frequency of 824 MHz and bandwidth of 144 MHz), with the upper half of the FRB emission (where the dispersion delay is less) already falling outside the voltage buffer. We followed standard CRAFT procedures for calibrating and imaging both the FRB and background continuum sources (Day et al. 2020), but flagged channels in which the FRB was not present for the FRB image only.

To refine the astrometric position of FRB 191001, we compared the positions of sources identified in the CRAFT image of the FRB field with reference positions obtained from the Australia Telescope Compact Array (ATCA) at 2 GHz, which is the closest we could get compared to ASKAP's FRB observation at 824 MHz. We did not use the full ASKAP observation as a reference due to the known arcsecond level astrometric uncertainties in ASKAP pilot data (Bhandari et al. 2018a). The process involved observation of three bright calibrators around the FRB field, namely, SUMSS J212104 −611125, SUMSS J213520−500652, and SUMSS J220054 −552008, and three continuum sources detected in the ASKAP

[13] This was caused by a software bug that has since been corrected.

image of the field generated from the 3 s of data containing the FRB, namely, J2132−5420, J2134−5450, and J2140−5455 at 824 MHz. The phase calibration solutions were derived using each of the calibrator sources and transferred to the background continuum sources and other calibrators. Out of three calibrators, the solutions derived from SUMSS J213520−500652 resulted in zero positional offsets between the known and derived positions (from ATCA image) of calibrators within positional uncertainties. Thus, SUMSS J213520−500652 was used for the remainder of this analysis.

The position of background sources obtained from the ATCA radio image were compared with the ASKAP field source positions, and we obtain a weighted mean systematic offset (also described in Macquart et al. 2020) of 731 ± 165 mas in R.A. and −809 ± 127 mas in decl. These corrections were applied to the position of the FRB and final uncertainties were obtained by taking a quadrature sum of systematic and statistical uncertainties. The FRB position is R.A.(J2000): 21:33:24.373(6) and decl. (J2000): −54:44:51.86(13).

### 2.4. DM Excess

The observed DM of the FRB can be broken down into contributions from various components as

$$\mathrm{DM_{obs}} = \mathrm{DM_{ISM}} + \mathrm{DM_{MW,halo}} + \mathrm{DM_{cosmic}} + \mathrm{DM_{host}}, \quad (1)$$

where $\mathrm{DM_{ISM}}$ is estimated to be 44 pc cm$^{-3}$ and 31 pc cm$^{-3}$ from the Galactic models of NE2001 (Cordes & Lazio 2002) and YMW16 (Yao et al. 2017), respectively; the contributions from the Milky Way halo and the host galaxy are $\mathrm{DM_{MW,halo}} = 50$ pc cm$^{-3}$ and $\mathrm{DM_{host}} = 50/(1+z) = 40$ pc cm$^{-3}$, respectively, following the assumptions presented in Macquart et al. (2020). This leaves the budget for DM from the intergalactic medium (IGM) to be $\mathrm{DM_{cosmic}} = 373(386)$ pc cm$^{-3}$ using the NE2001 (YMW16) models. Based on predictions from the Macquart relation (Macquart et al. 2020), we would expect $\mathrm{DM_{cosmic}}$ to be 203 pc cm$^{-3}$, which is significantly lower than the value of $\mathrm{DM_{cosmic}}$ inferred from the observed DM and assumptions for $\mathrm{DM_{MW,halo}}$ and $\mathrm{DM_{host}}$. Thus, as for FRB 190608 (Chittidi et al. 2020) and FRB 121102 (Tendulkar et al. 2017), it is likely that FRB 191001 has a larger host contribution than typical, or lies along a sight line that traces a denser-than-average path through the cosmic web (Simha et al. 2020). The host DM contribution can also be probed by optical studies. We use the relation between optical reddening $E(B-V)$ and hydrogen column density $N_{\mathrm{H}}$ from Güver & Özel (2009), together with the DM–$N_{\mathrm{H}}$ correlation of He et al. (2013) to estimate the DM contribution from the host of FRB 191001. We find $\mathrm{DM_{host}} = 61$ pc cm$^{-3}$, which is higher than our previous assumption but still leads to an excess in the cosmic DM. A more detailed discussion of the breakdown of the excess DM for this FRB is beyond the scope of this Letter, and will be considered in a future work.

### 2.5. High-time-resolution Analysis

We performed a high-time-resolution analysis of the FRB using the CRAFT voltage data. Data were beam-formed (i.e., coherently summed) at the position of the FRB using the delay, bandpass, and phase solutions derived from the calibrator source PKS 0407−658. The 144 1 MHz bandwidth ASKAP channels that contained signal from the FRB were then coherently de-dispersed at the FRB DM before being passed through a synthesis filter to reconstruct a single 144 MHz channel with ∼7 ns time resolution. A detailed description of the high-time-resolution construction process is given by Cho et al. (2020).

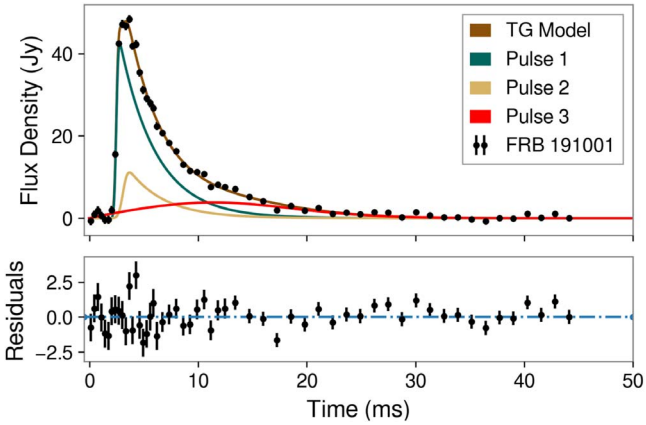


**Figure 3.** Pulse morphology model fit using 64 $\mu$s time series. The best-fit model comprises three scatter-broadened components. The residuals are shown in the panel below. The data points between 0–6 ms, 6–25 ms, and 25–50 ms are averaged by a factor of 5, 10, and 20, respectively, for display.

We determined the scintillation bandwidth ($\delta\nu_d$) using a range of time bins in the FRB dynamic spectrum (encompassing roughly the half-power points of the pulse), with a frequency resolution of 7.812 kHz, by performing an auto-correlation function (ACF) analysis following Cho et al. (2020). We estimate $\delta\nu_d \sim 600$ kHz, which is consistent with expectations for diffractive scintillation (DISS) from the Milky Way along the burst line of sight at this frequency using the NE2001 model (∼860 kHz).

We fit the frequency-averaged pulse profile with scattered Gaussian pulse models using the nested sampling method presented in Qiu et al. (2020) and Cho et al. (2020) to compare the evidence for multiple pulse components as demonstrated in Day et al. (2020). Model comparison favors three scattered pulse components (TG model in Figure 3) by a Bayes factor of $\log_{10} B = 20$ to a single-pulse model and $\log_{10} B = 5$ to a double-pulse model with significantly lower rms error. The pulse width of components in order of appearance are $0.22 \pm 0.03$, $0.4 \pm 0.2$, and $9 \pm 2$ ms, respectively. We measure an exponential broadening of $3.3 \pm 0.2$ ms at 824 MHz. The second and third pulse components occur $0.6 \pm 0.2$ and $5.9 \pm 1.2$ ms after the first pulse (see Figure 3). The presence of further components or frequency-dependent structure could plausibly explain the remaining structure in the residuals in Figure 3.

#### 2.5.1. Spectro-temporal Polarization Properties

The time series was time-averaged to a resolution of 32 $\mu$s for polarization analysis (Figure 1). The polarization calibration was performed by comparing an ASKAP observation of the Vela pulsar with an observation obtained with the Parkes radio telescope for which an accurate polarization calibration exists, as described in Day et al. (2020). Unlike some earlier FRBs detected by ASKAP, there is negligible leakage between Stokes $U$ and $V$ as a result of polarization leakage correction in the beam weight calculation.[14]

[14] https://www.atnf.csiro.au/projects/askap/ASKAP_com_update_v32.pdf

We used the RMFIT program in the PSRCHIVE software package (Hotan et al. 2004) to calculate the rotation measure (RM) of FRB 191001. RMFIT performs a search for peak linear polarization as a function of trial RM. We find the best-fit RM for FRB 191001 to be $55.5 \pm 0.9$ rad m$^{-2}$.

In addition, we estimated polarization fractions integrated over the FRB pulse using the PSRCHIVE software package. The values for total, linear, and circular polarization fractions are presented in Table 1. These values are lower than the values observed for the sample of ASKAP FRBs discussed in Day et al. (2020) and Cho et al. (2020). We also note that the circular (Stokes $V$) peaks later than the linear polarization.

The left panel of Figure 1 shows the Stokes parameter profiles and polarization position angle (PA) for FRB 191001, with a time resolution of 32 $\mu$s. As noted above, the pulse is not consistent with a single Gaussian component convolved with an exponential scattering tail—indicating the presence of multiple components blended in the scattering tail (as proposed in Day et al. 2020 for FRB 180924 and FRB 190608). We observe a pulse rise time of $\sim$640 $\mu$s by counting the number of samples from 1$\sigma$ to the peak value. Also, the PA is initially flat across the majority of the pulse (as shown in the top left panel of Figure 1), which is possibly a consequence of scattering that not only affects the shape of the total intensity pulse profile but also measured polarization properties (Caleb et al. 2018). At later times, the noise in the PA makes it difficult to establish whether the second component has a position angle that differs substantially from the scattering tail of the first component. It is suggestive that the largest deviations from a constant PA are seen at this time.

The absence of variation in the PA across the main pulse and the scatter-blended multiple components observed in FRB 191001 bear a remarkable resemblance to FRB 180924 and FRB 190608 (Day et al. 2020). The separation between the three modeled components for FRB 191001, however, greatly exceeds that of the other bursts. Of note, although observed at different frequencies, the three FRBs exhibit similar substructure in the residuals in the scattering tail.

### 2.6. Host Galaxy of FRB 191001

The host galaxy of FRB 191001 was identified as DES J213324.44−544454.18, a galaxy cataloged in the Dark Energy Survey (DES; Abbott et al. 2018). Spectroscopic observations conducted on 2019 October 4 UT using the Gemini Multi-Object Spectrograph (GMOS) on the Gemini-South telescope established the redshift of the host to be $z = 0.2340(1)$ using the H$\beta$ spectral line (see Heintz et al. 2020 for further details). On 2019 October 5 UT deep optical imaging observations were performed with the FOcal Reducer and low dispersion Spectrograph 2 (FORS2) instrument on the Very Large Telescope (VLT). The left panel of Figure 2 shows the $g$-band image of the host, which is clearly a spiral galaxy. The neighboring galaxy, DES J213323.65−544453.6, is also at a similar redshift ($z = 0.2339(2)$), hence the system is a double and possibly interacting pair of galaxies. Detailed optical properties of the host are described in Heintz et al. (2020).

### 2.7. Radio Properties of the Host Galaxy

We conducted observations with ATCA (project code C3211) in a 6 km array configuration to search for radio emission from the FRB 191001 host galaxy at 5.5 GHz and 7.5 GHz. Observations were performed in three epochs starting 2020 January 24, 2020 March 6, and 2020 March 12 at different hour angles to maximize ($u$, $v$)-coverage. Epoch 1 was badly affected by weather and therefore discarded. We later obtained a fourth epoch on 2020 April 16 (project code C3347) at 2, 5.5, and 7.5 GHz. We combined epoch 2, epoch 3, and epoch 4 data in the 4 cm band for deep imaging. However, we use only epoch 4 data for estimating source flux densities.

**Table 2**
Integrated Flux Densities for the Host of FRB 191001 and Neighboring Western Source Derived from Epoch 4

| | | Host | Western Source |
|---|---|---|---|
| Freq. (GHz) | rms ($\mu$Jy beam$^{-1}$) | $S_{\rm int}$ ($\mu$Jy) | $S_{\rm int}$ ($\mu$Jy) |
| 2 | 30 | 241 ± 2 | 509 ± 2 |
| 5.5 | 11 | 103 ± 1 | 246 ± 2 |
| 7.5 | 10 | 123 ± 2 | 208 ± 1 |

**Note.** The flux densities and uncertainties were estimated using imfit in miriad at 5.5 and 7.5 GHz images, smoothed to a common resolution ($4\farcs7 \times 3\farcs4$, PA $= -1\fdg8$).

#### 2.7.1. Search for Persistent Emission

We used the obtained ATCA data to search for a compact persistent radio source that may be associated with FRB 191001. We detect low-level diffuse radio emission with a peak flux density of $\sim$15 $\mu$Jy beam$^{-1}$ at the FRB position pixel, corresponding to a luminosity of $2.1 \times 10^{21}$ W Hz$^{-1}$ at 5.5 GHz. This luminosity is an order of magnitude less than the luminosity of the persistent source observed for FRB 121102 (Chatterjee et al. 2017). We did not find a compact persistent radio source co-located with FRB 191001 above a flux density of 15 $\mu$Jy.

#### 2.7.2. Star Formation in the Host Galaxy

We detect radio emission from the host of FRB 191001 (H) and the western source (W) as shown in the left panel of Figure 2. For estimating the integrated flux densities, we smoothed the images at respective frequencies to the same angular resolution—smoothing beam resolution at 7.5 GHz ($1\farcs7 \times 1\farcs2$, PA $= 2\fdg1$) and 5.5 GHz ($2\farcs3 \times 1\farcs7$, PA $= 2\fdg2$) to 2 GHz ($4\farcs7 \times 3\farcs4$, PA $= -1\fdg8$) resolution. The flux densities for both sources were measured using the miriad task imfit on the smoothed version of radio images and fixing the beam to the size of the common resolution, i.e., $4\farcs7 \times 3\farcs4$, PA $= -1\fdg8$. Flux densities are presented in Table 2. We note an excess emission at 7.5 GHz to the southeast of the host galaxy. This resolved flat-spectrum component overlapping with the southeast spiral arm of the galaxy (see Figure 2) could indicate the presence of thermal emission associated with (possibly ongoing) star formation along the spiral arm. Further discussion will be presented in an upcoming paper.

Next, a spectral index map was obtained using the same resolution images at 2 GHz and 5.5 GHz. We find the spectral index ($\alpha$), where $S_\nu \propto \nu^\alpha$, for the host varies from $-1.0$ at the outer edges to $-0.8$ at the center. Hence, the lack of much flattening ($\alpha > -0.7$) of the spectral index near the nucleus suggests no evidence for a dominant compact AGN. We further fit a power law to the integrated flux densities (excluding 7.5 GHz for the host) and find their spectral indices to be

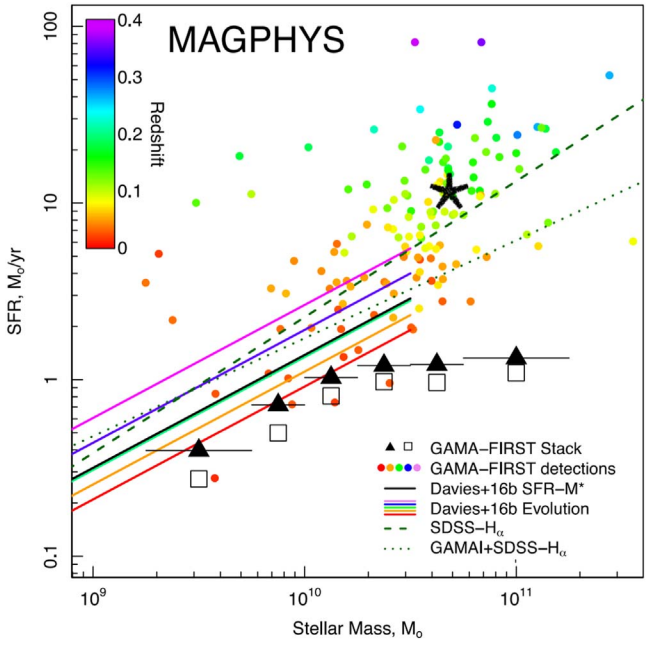


**Figure 4.** The 1.4 GHz SFR$-M^*$ relation. We show the relation derived from GAMA galaxies, derived using the free-fit luminosity-to-SFR relation for MAGPHYS. The black star is the host of FRB 191001 overplotted on a sample of galaxies at various redshifts detected in the GAMA survey. Figure adapted from Figure 5 of Davies et al. (2017).

$\alpha_H = -0.8$ and $\alpha_W = -0.7$, respectively. The diffuse morphology and steep negative spectral index suggest that the radio emission (or most of the emission seen in the host) is dominated by synchrotron emission due to star formation (SF) in the galaxy. We note that the current resolution observations do not rule out contamination from a low-level AGN emission.

Furthermore, we estimate an inferred star formation rate (SFR) using a new 1.4 GHz luminosity-to-SFR relation derived combining the data from the Galaxy And Mass Assembly (GAMA) survey and the Faint Images of the Radio Sky at Twenty-cm (FIRST) survey (Davies et al. 2017). The new robust calibration to the 1.4 GHz−SFR relation is given by

$$\log_{10}[\mathrm{SFR}(M_\odot\ \mathrm{yr}^{-1})] = M \times \log_{10}[L_{1.4\,\mathrm{GHz}}(\mathrm{W\ Hz}^{-1})] + C, \quad (2)$$

where parameters $M = 0.75 \pm 0.03$ and $C = -15.96 \pm 0.58$ for corrections based on the MAGPHYS SFRs in the GAMA work and $L_{1.4}$ is the radio luminosity at 1.4 GHz. We find the star formation rate of the host to be $\mathrm{SFR_{MAGP}} = 11.2\,M_\odot\,\mathrm{yr}^{-1}$ and that the host of FRB 191001 is consistent with the underlying population of galaxies at a similar redshift in the GAMA sample (see Figure 4). A possible caveat is the potential for contamination of a low-level AGN in our star formation rate calculations. Assuming the source is dominated by SF gives us an upper limit on the SFR.

A high SFR qualifies this galaxy as starburst or experiencing interaction-triggered bursts of star formation similar to the NGC4038/4039 pair of galaxies a.k.a. The Antennae (Whitmore et al. 1995). We note that the host of FRB 191001 has the highest SFR in the ASKAP sample (Heintz et al. 2020), suggesting diversity in galaxies hosting FRBs.

## 3. Search for Radio Afterglows

### 3.1. Low-time-resolution Data

We performed a search for repeats and afterglows at the position of FRB 191001. First, a deep image of the field was made using ASKAP low-time-resolution data taken ∼8 hr prior to the FRB observation. A model of background sources was created using the CASA task TCLEAN and subtracted from all ASKAP data using UVSUB. Second, the visibilities were rotated in phase to the position of the FRB to extract the dynamic spectra. Finally, we obtained a light curve for ∼9 hr of data (see the left panel of Figure 5) by averaging baselines of the source-model-subtracted and phase-rotated data. We also subtracted the underlying host radio emission from the light curve. The peak in the light curve (Stokes $I$) is the emission from the FRB.

We averaged the light curve over boxcar widths of $2^N$, where $N$ varies from 0 to 9, to search for slowly varying radio emission on timescales ranging from 10 s to 1.4 hr. The data show red noise either due to contamination by sidelobes of poorly subtracted faint sources in the image domain, radio frequency interference, or residual emission from the host of FRB 191001 (see the top panel of Figure 6), and is therefore not amenable to a chi-square test that assumes statistically independent (white) samples. By eye, we find no evidence for slowly varying radio emission at the FRB position ∼8 hr before and ∼1 hr after FRB 191001 above a $5\sigma$ flux density limit at respective timescales as presented in Table 3.

### 3.2. High-time-resolution Data

We also performed a search for dispersed radio emission pre-/post-FRB in ∼3 s of CRAFT high-time-resolution data (presented in Section 2.5). We time-averaged the beam-formed data to 1 ms (see the right panel of Figure 5) to obtain an initial time series, which was further averaged over boxcar widths $2^N$, where $N$ varies from 0 to 9. This allowed a search for varying radio emission on timescales ranging from 1 to 512 ms. Analysis of the noise showed it to be Gaussian distributed with no frequency dependence (i.e., white noise). Therefore, we performed a chi-square analysis to test the null hypothesis that there is a slowly varying radio emission pre-/post-FRB. The measured chi-square ($\chi^2_{\mathrm{M}}$) is given by

$$\chi^2_{\mathrm{M}} = \sum_{i=0}^{i=n} \frac{(Y_i - Y_{\mathrm{mean}})^2}{\sigma_i^2}, \quad (3)$$

where $Y_i$ is the flux density for boxcar width $i$, $Y_{\mathrm{mean}}$ is the mean flux density of the time series, and $\sigma_i$ is the standard deviation of the off-pulse time series scaled as $\sigma_i = \sigma_0/\sqrt{i}$ ($\sigma_0$ is the standard deviation of the subtracted FRB time series with zero boxcar width and $i = 2^N$, where $N$ varies from 0–9). We calculated the cumulative distribution function and the probability $P$ of obtaining a measured chi-square ($\chi^2_{\mathrm{M}}$) by chance and compared it with the critical chi-square ($\chi^2_{\mathrm{crit}}$) for $N$ degrees of freedom. Variable radio emission exists if $\chi^2_{\mathrm{M}} > \chi^2_{\mathrm{crit}}$ for $P < 0.02$ (98% confidence level). In our data, the $\chi^2_{\mathrm{M}}$ for each boxcar width was less than $\chi^2_{\mathrm{crit}}$. Therefore, we rejected the null hypothesis that varying radio emission exists at the 98% confidence level.

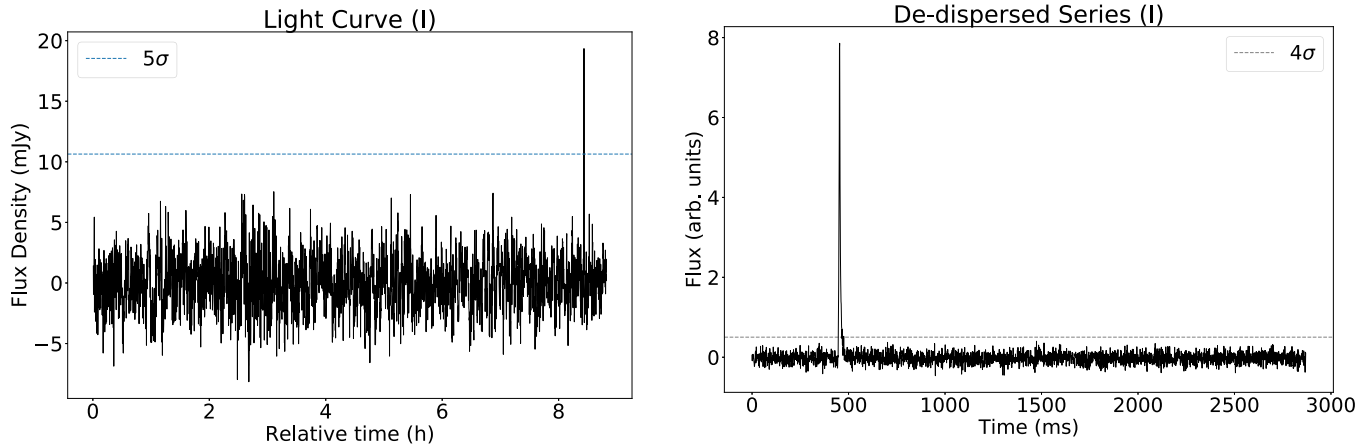


**Figure 5.** Left: ASKAP light curve obtained at the position of the FRB on a timescale of 10 s for an ∼9 hr observation of the EMU field. FRB 191001 was detected at UT 16:55:35.97081 in ASKAP low-time-resolution data. Right: ASKAP light curve on a timescale of 1 ms derived by beam-forming CRAFT data, de-dispersed at the DM of the FRB.

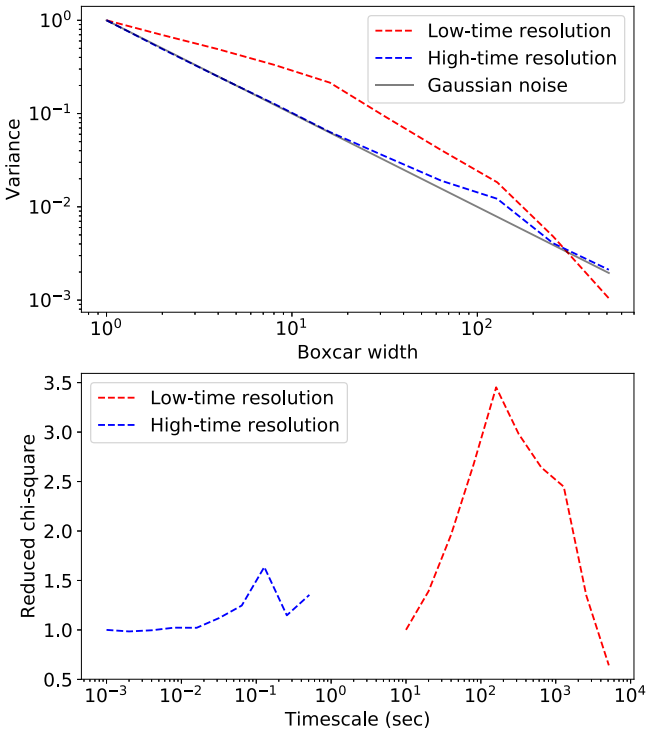


**Figure 6.** Top panel: plot of variance vs. boxcar width for ASKAP low-time-resolution series (red) and CRAFT high-time-resolution series (blue) after subtracting FRB 191001. This plot shows that the Gaussian noise in low-time-resolution series data does not vary linearly with boxcar width (as expected for white Gaussian noise). Bottom panel: plot of reduced chi-square vs. timescales under investigation assuming a white Gaussian noise. No varying radio emission was observed in the low-time-resolution data light curve above $5\sigma$. The high value of reduced chi-square is due to systematics. A chi-square test on high-time-resolution series data rejects the hypothesis that varying radio emission exists at 98% confidence.

**Table 3**
$5\sigma$ Flux Density and Limits on Luminosities for Radio Emission at Different Timescales at the Position of the FRB

| Timescale (s) | Flux Limit (mJy beam$^{-1}$) | Luminosity (W Hz$^{-1}$) |
|---|---|---|
| 10 | 10.64 | $1.50 \times 10^{24}$ |
| 20 | 8.87 | $1.25 \times 10^{24}$ |
| 40 | 7.44 | $1.05 \times 10^{24}$ |
| 80 | 6.14 | $8.67 \times 10^{23}$ |
| 160 | 4.93 | $6.95 \times 10^{23}$ |
| 320 | 3.23 | $4.56 \times 10^{23}$ |
| 640 | 2.14 | $3.02 \times 10^{23}$ |
| 1280 | 1.44 | $2.03 \times 10^{23}$ |
| 2560 | 0.74 | $1.04 \times 10^{23}$ |
| 5120 | 0.34 | $4.85 \times 10^{22}$ |

## 4. Discussion

### 4.1. FRBs as Image-plane Transients

Here we consider the viability of detecting FRBs as image-plane transients in 10 s snapshot images with ASKAP. A $5\sigma$ detection in a 10 s ASKAP snapshot would be very difficult to confirm. We use $10\sigma$ or flux density greater than 20 mJy (robust = 0.5 weighting) as a reasonable threshold, which should lead to minimal false positives. Of the CRAFT sample of 25 FRBs discovered in fly's eye mode (Shannon et al. 2018; Bhandari et al. 2019; Qiu et al. 2019), 3 have flux densities greater than 20 mJy, when diluted to 10 s integration time. Thus, 3 out of 25 FRBs would have been detected as reliable image-plane transients. Scaling the ASKAP all-sky rate, $R(>26\,\mathrm{Jy\,m\,s\,(w/1.26\,m\,s)^{-1/2}})$ of 37 sky$^{-1}$ day$^{-1}$ (Shannon et al. 2018), we derive an FRB rate, $R$ (>20 mJy, 10 s) of 4.4 FRBs sky$^{-1}$ day$^{-1}$ or 0.00011 deg$^{-2}$ day$^{-1}$. We compare this rate with other slow transients in Table 4. A scaling of $N \propto S^{-3/2}$ has been used to scale the rate of various slow transients above a flux density threshold of 0.3 mJy in Mooley et al. (2016) to the ASKAP flux density limit of 20 mJy. The FRB transients are more common than all other slow transients except the AGN(ISS) and the only transients expected on 10 s timescale.

*How useful is a 10 s search of ASKAP data?* The 10 s data search is affordable as compared to searching at different DM trials. However, DM searching would not be possible to confirm candidates as the dispersion delay is typically $\ll$10 s for FRBs less than a DM of $\sim$2000 pc cm$^{-3}$ at 920 MHz. Additionally, the existing incoherent-sum (ICS) CRAFT search system can find FRBs more effectively. The signal-to-noise ratio (S/N) in the 10 s data is improved by $\sqrt{N}$, where $N$ is the number of antennas, but diluted by $\sqrt{(10\,\mathrm{s/FRB\_width})}$. For instance, a $100\sigma$ FRB of width 1 ms in ICS mode with $N = 36$

**Table 4**
Rates of the Slow Radio Transients at ASKAP Snapshot Sensitivity Modified from Mooley et al. (2016)

| Object | Timescale | Rate (>20 mJy) ($deg^{-2}$) |
|---|---|---|
| AGN (ISS) | minutes−days | 0.110 |
| Active star (flaring) | hr−days | $3.7 \times 10^{-5}$ |
| Active binary (flaring) | hr−days | $1.8 \times 10^{-5}$ |
| CVs (dwarf nova/jet) | hr−days | $1.8 \times 10^{-6}$ |
| YSO (mass accretion/flare) | hr−weeks | $<9.1 \times 10^{-5}$ |
| Brown dwarfs (pulsing) | s−hr | $<9.1 \times 10^{-5}$ |

**Note.** The slow transient sources include interstellar scintillation (ISS) of an AGN, active star flaring, cataclysmic variables (CVs), young stellar object (YSO), and brown dwarfs. These transients may vary on timescales of seconds to weeks.

antennas will be a $6\sigma$ detection in ASKAP low-time-resolution imaging mode; hence ICS mode is significantly more sensitive than the ASKAP imaging mode. Nevertheless, we encourage searches for transients at shorter timescales at other interferometric sites that lack CRAFT-like system for potential FRB detection.

### 4.2. Constraints on Afterglows

Wang & Lai (2020) have predicted radio afterglows for models involving an NS, WD, or BH as the central engines, finding that sub-mJy level afterglows for nonrepeating FRBs peak around 10 days post-burst at 1 GHz. For a binary NS merger scenario, the $\mu$Jy level peak of the radio afterglow light curves of the jet (at different viewing angles) and isotropic ejecta at 1.4 GHz from a source at $z = 0.5$ may vary on timescales of a few days to years (Lin & Totani 2020). For a magnetar produced in a binary NS merger and AIC of a white dwarf, a late-time radio emission (from months/years to decades depending on the triggering mechanism) is anticipated (Margalit et al. 2019).

Most of these models predict FRB afterglows on timescales of months to years, longer than our observations probe. More interestingly for our study, Yi et al. (2014) present light curves for both forward- and reverse-shock afterglows on timescales of seconds to days post-burst. They used the standard fireball model for GRB afterglows to estimate luminosities of FRB radio afterglows for a range of assumed total kinetic energies and redshifts. Their models predict radio emission with post-burst flux densities <1 mJy for burst redshifts between 0.01 to 0.5 at 1 GHz. Our 920 MHz ASKAP data probe these timescales but the predicted fluxes are well below our search threshold of 10 mJy for a $5\sigma$ detection of radio emission from an FRB at $z = 0.2340(1)$, consistent with our nondetection of afterglows in low-time-resolution data spanning the hour after the FRB.

Our luminosity limits are presented in Table 3. Detection of energetic and low-redshift FRBs ($z = 0.1$–$0.01$) in commensal ASKAP-CRAFT observations will place stronger constraints on the radio radiative efficiency of this model or could lead to detection. Constraints on long-lasting, persistent, or variable radio emission associated with FRBs will require a long-term monitoring program of FRB host galaxies on a day to year timescales.

## 5. Summary

We report the detection of the first commensal FRB with ASKAP, FRB 191001, at 920 MHz. Simultaneous imaging with the ASKAP hardware correlator led to a search for slowly varying radio emissions before, during, and after the FRB. We did not find a varying radio emission and report luminosity limits on timescales from 10 s to 1.4 hr, which could potentially be used to constrain progenitor models predicting FRB afterglows. We also demonstrate that bright FRBs can be detected as image-plane transients.

FRB 191001 is the brightest burst that has the best localization among the sample of seven ASKAP localized FRBs (Macquart et al. 2020). The FRB originates from the outskirts of a star-forming spiral galaxy in a possibly interacting double system at a redshift of 0.2340(1). Radio observations of the host galaxy reveal no compact persistent radio source associated with FRB 191001 above 15 $\mu$Jy. However, the host is radio luminous with most of the synchrotron radio emission occurring due to high star formation in the galaxy.

FRB 191001 shows multiple burst components, a large scattering tail, and a flat polarization position angle. These properties bear similarities with FRB 180924 and FRB 190608 (Day et al. 2020). While the FRB is hosted in a star-forming galaxy, the low Faraday rotation hints at a progenitor environment not dominated by high magnetic fields.

The commensal observations of ASKAP-CRAFT with the imaging mode will continue to explore prompt radio emissions and afterglows associated with FRBs (if any), making ASKAP a unique and a powerful instrument in the studies of FRBs and their progenitor systems.

S.B. would like to thank Manisha Caleb for discussions about polarization of FRB 191001. Based on observations collected at the European Southern Observatory under ESO program 0103.A-0101(A). K.W.B., J.P.M., and R.M.S. acknowledge Australian Research Council (ARC) grant DP180100857. A.T.D. is the recipient of an ARC Future Fellowship (FT150100415). R.M.S. is also the recipient of an ARC Future Fellowship (FT190100155). J.X.P., as a member of The Fast and Fortunate for FRB Follow-up team, acknowledges support from NSF grants AST-1911140 and AST-1910471. N.T. acknowledges support by FONDECYT grant 11191217. The Australian Square Kilometre Array Pathfinder is a part of the Australia Telescope National Facility, which is managed by CSIRO. Operation of ASKAP is funded by the Australian Government with support from the National Collaborative Research Infrastructure Strategy. ASKAP uses the resources of the Pawsey Supercomputing Centre. Establishment of ASKAP, the Murchison Radio-astronomy Observatory, and the Pawsey Supercomputing Centre are initiatives of the Australian Government, with support from the Government of Western Australia and the Science and Industry Endowment Fund. We acknowledge the Wajarri Yamatji as the traditional owners of the Murchison Radio-astronomy Observatory site. The Australia Telescope Compact Array is part of the Australia Telescope National Facility which is funded by the Australian Government for operation as a National Facility managed by CSIRO. We acknowledge the Gomeroi people as the traditional owners of the Observatory site. The Gemini-S/GMOS observations were carried out as part of program GS-2019B-Q-132, obtained at the international Gemini Observatory, a program of NSF's OIR Lab, which is managed by the Association of Universities for Research in Astronomy (AURA) under a

cooperative agreement with the National Science Foundation, on behalf of the Gemini Observatory partnership: the National Science Foundation (United States), National Research Council (Canada), Agencia Nacional de Investigación y Desarrollo (Chile), Ministerio de Ciencia, Tecnología e Innovación (Argentina), Ministério da Ciência, Tecnologia, Inovações e Comunicações (Brazil), and Korea Astronomy and Space Science Institute (Republic of Korea).

## ORCID iDs

Shivani Bhandari https://orcid.org/0000-0003-3460-506X
Keith W. Bannister https://orcid.org/0000-0003-2149-0363
Emil Lenc https://orcid.org/0000-0002-9994-1593
Hyerin Cho https://orcid.org/0000-0002-2858-9481
Ron Ekers https://orcid.org/0000-0002-3532-9928
Cherie K. Day https://orcid.org/0000-0002-8101-3027
Adam T. Deller https://orcid.org/0000-0001-9434-3837
Chris Flynn https://orcid.org/0000-0002-4796-745X
Clancy W. James https://orcid.org/0000-0002-6437-6176
Jean-Pierre Macquart https://orcid.org/0000-0001-6763-8234
Elizabeth K. Mahony https://orcid.org/0000-0002-5053-2828
Lachlan Marnoch https://orcid.org/0000-0003-1483-0147
Vanessa A. Moss https://orcid.org/0000-0002-3005-9738
Hao Qiu https://orcid.org/0000-0002-9586-7904
Stuart D. Ryder https://orcid.org/0000-0003-4501-8100
Ryan M. Shannon https://orcid.org/0000-0002-7285-6348
Nicolas Tejos https://orcid.org/0000-0002-1883-4252
O. Ivy Wong https://orcid.org/0000-0003-4264-3509

## References

Abbott, T. M. C., Abdalla, F. B., Allam, S., et al. 2018, ApJS, 239, 18
Andersen, B. C., Bandura, K., Bhardwaj, M., et al. 2019, ApJL, 885, L24
Bannister, K. W., Deller, A. T., Phillips, C., et al. 2019, Sci, 365, 565
Bhandari, S., Bannister, K. W., James, C. W., et al. 2019, MNRAS, 486, 70
Bhandari, S., Bannister, K. W., Murphy, T., et al. 2018a, MNRAS, 478, 1784
Bhandari, S., Keane, E. F., Barr, E. D., et al. 2018b, MNRAS, 475, 1427
Bhandari, S., Sadler, E. M., Prochaska, J. X., et al. 2020, ApJL, 895, L37
Caleb, M., Keane, E. F., van Straten, W., et al. 2018, MNRAS, 478, 2046
Chatterjee, S., Law, C. J., Wharton, R. S., et al. 2017, Natur, 541, 58
Chittidi, J. S., Simha, S., Mannings, A., et al. 2020, arXiv:2005.13158
Cho, H., Macquart, J.-P., Shannon, R. M., et al. 2020, ApJL, 891, L38
Cordes, J. M., & Lazio, T. J. W. 2002, arXiv:astro-ph/0207156
Davies, L. J. M., Huynh, M. T., Hopkins, A. M., et al. 2017, MNRAS, 466, 2312
Day, C. K., Deller, A. T., Shannon, R. M., et al. 2020, MNRAS, 497, 3335
Frail, D. A. 2003, arXiv:astro-ph/0309557
Güver, T., & Özel, F. 2009, MNRAS, 400, 2050
He, C., Ng, C. Y., & Kaspi, V. M. 2013, ApJ, 768, 64
Heintz, K., Prochaska, X. J., Simha, S., et al. 2020, ApJ, in press
Hotan, A. W., van Straten, W., & Manchester, R. N. 2004, PASA, 21, 302
Johnston, S., Keane, E. F., Bhandari, S., et al. 2017, MNRAS, 465, 2143
Keane, E., Johnston, S., Bhandari, S., et al. 2016, Natur, 530, 453
Kumar, P., Shannon, R. M., Osłowski, S., et al. 2019, ApJL, 887, L30
Law, C. J., Butler, B. J., Prochaska, J. X., et al. 2020, ApJ, 899, 161
Lin, H., & Totani, T. 2020, MNRAS, in press (doi:10.1093/mnras/staa2418)
Liu, T., Romero, G. E., Liu, M.-L., & Li, A. 2016, ApJ, 826, 82
Liu, X. 2018, Ap&SS, 363, 242
Lorimer, D. R., Bailes, M., McLaughlin, M. A., Narkevic, D. J., & Crawford, F. 2007, Sci, 318, 777
Macquart, J.-P., Bailes, M., Bhat, N. D. R., et al. 2010, PASA, 27, 272
Macquart, J. P., Prochaska, J. X., McQuinn, M., et al. 2020, Natur, 581, 391
Marcote, B., Nimmo, K., Hessels, J. W. T., et al. 2020, Natur, 577, 190
Margalit, B., Berger, E., & Metzger, B. D. 2019, ApJ, 886, 110
Mooley, K. P., Hallinan, G., Bourke, S., et al. 2016, ApJ, 818, 105
Murase, K., Toomey, M. W., Fang, K., et al. 2018, ApJ, 854, 60
Norris, R. P., Hopkins, A. M., Afonso, J., et al. 2011, PASA, 28, 215
Prochaska, J. X., Macquart, J.-P., McQuinn, M., et al. 2019, Sci, 366, 231
Qiu, H., Bannister, K. W., Shannon, R. M., et al. 2019, MNRAS, 486, 166
Qiu, H., Shannon, R. M., Farah, W., et al. 2020, MNRAS, 497, 1382
Ravi, V., Catha, M., D'Addario, L., et al. 2019, Natur, 572, 352
Shannon, R. M., Macquart, J.-P., Bannister, K. W., et al. 2018, Natur, 562, 386
Simha, S., Burchett, J. N., Prochaska, J. X., et al. 2020, arXiv:2005.13157
Spitler, L., Scholz, P., Hessels, J., et al. 2016, Natur, 531, 202
Tendulkar, S. P., Bassa, C. G., Cordes, J. M., et al. 2017, ApJL, 834, L7
Tendulkar, S. P., Kaspi, V. M., & Patel, C. 2016, ApJ, 827, 59
Wang, F. Y., Wang, Y. Y., Yang, Y.-P., et al. 2020, ApJ, 891, 72
Wang, J.-S., & Lai, D. 2020, ApJ, 892, 135
Whitmore, B. C., Sparks, W. B., Lucas, R. A., Macchetto, F. D., & Biretta, J. A. 1995, ApJL, 454, L73
Williams, P. K. G., & Berger, E. 2016, ApJL, 821, L22
Yao, J. M., Manchester, R. N., & Wang, N. 2017, ApJ, 835, 29
Yi, S.-X., Gao, H., & Zhang, B. 2014, ApJL, 792, L21
Zhang, B. 2014, ApJL, 780, L21